OPEN ACCESS



Distribution of H α Emitters in Merging Galaxy Clusters

David Wittman ¹, Dariush Imani ¹, Rutger Hartmann Olden ¹, and Nathan Golovich ², Department of Physics & Astronomy, University of California, Davis, CA 95616, USA; dwittman@physics.ucdavis.edu ² Lawrence Livermore National Laboratory, 7000 East Avenue, Livermore, CA 94550, USA Received 2023 February 3; revised 2023 September 22; accepted 2023 October 12; published 2024 January 9

Abstract

Studies of star formation in various galaxy cluster mergers have reached apparently contradictory conclusions regarding whether mergers stimulate star formation, quench it, or have no effect. Because the mergers studied span a range of time since pericenter (TSP), it is possible that the apparent effect on star formation is a function of the TSP. We use a sample of 12 bimodal mergers to assess the star formation as a function of TSP. We measure the equivalent width of the H α emission line in \sim 100 member galaxies in each merger, classify galaxies as emitters or nonemitters, and then classify emitters as star-forming galaxies (SFGs) or active galactic nucleus (AGN) based on the [N II] λ 6583 line. We quantify the distribution of SFG and AGN relative to nonemitters along the spatial axis defined by the subcluster separation. The SFG and AGN fractions vary from merger to merger but show no trend with TSP. The spatial distribution of SFG is consistent with that of nonemitters in eight mergers, but show significant avoidance of the system center in the remaining four mergers, including the three with the lowest TSP. If there is a connection between star formation activity and TSP, probing it further will require more precise TSP estimates and more mergers with TSP in the range of 0–400 Myr.

Unified Astronomy Thesaurus concepts: Galaxy clusters (584); Star formation (1569) Supporting material: machine-readable table

1. Introduction

A merger of galaxy clusters provides an important astrophysical laboratory for probing the behavior of dark matter and the hot gas in the intracluster medium; see Molnar (2016) for a review. Studies conflict on whether mergers stimulate star formation (Miller & Owen 2003; Ma et al. 2010; Sobral et al. 2015; Stroe et al. 2017), suppress it (Mansheim et al. 2017b), or have no substantial effect (Chung et al. 2010). These studies typically focus on a single merger or two, with some comparison to field galaxies at comparable redshift. Hence, the disparate results are potentially consistent with mergers having a variable effect depending on dynamical parameters such as pericenter speed or the elapsed time between pericenter and the observed state, or time since pericenter (TSP). If star formation is stimulated promptly then later quenched, for example, observations of various mergers will naturally lead to differing conclusions.

Testing this hypothesis requires a sample of mergers for which TSP can be inferred. The classic "timing argument" of Kahn & Woltjer (1959) uses equations of motion for two point masses on radial trajectories in an expanding universe. Further assumptions on the viewing angle allow one to compare this model to observables: the projected subcluster separation $d_{\rm proj}$ and the line-of-sight component of the relative velocity, $\Delta v_{\rm los}$. Dawson (2013) updated this idealized model by using Navarro–Frenk–White (Navarro et al. 1997) mass profiles rather than point masses, and by marginalizing over possible viewing angles while keeping in place the assumption of zero pericenter distance.

Original content from this work may be used under the terms of the Creative Commons Attribution 4.0 licence. Any further distribution of this work must maintain attribution to the author(s) and the title of the work, journal citation and DOI.

Wittman et al. (2018) and Wittman (2019) developed an approach that naturally incorporates a cosmologically motivated range of pericenter distances, as well as effects of substructure and surrounding structure. They identified postpericenter halo pairs in cosmological n-body simulations and placed mock observers to compute the joint likelihood of viewing angle and halo pair, given the observables d_{proj} and $\Delta v_{\rm los}$, as well as the subcluster masses if known. The joint likelihood can be marginalized over the viewing angle to obtain a likelihood for each simulated halo pair to serve as an analog for the observed system. Furthermore, each halo pair is tagged with a known TSP, obtained from prior snapshots of the cosmological simulation. This enables the calculation of likelihoods for TSP as well as other dynamical variables such as pericenter speed v_{max} and angle between velocity and separation vectors φ . Wittman (2019) noted that allowing for $\varphi \neq 0$, i.e., nonradial trajectories, removed a longstanding bias in TSP inference. In systems where any nonzero Δv_{los} is observed, the assumption of radial trajectories immediately rules out a subcluster separation vector in the plane of the sky. Real systems do have some tangential velocity component, so plane-of-sky separation vectors—the most likely configuration a priori—are falsely ruled out under the radial trajectory assumption; this leads to a bias toward larger 3D separations, hence larger TSP.

Merging cluster samples have grown in size and quality as well. Golovich et al. (2019a, hereafter G19a) conducted an optical and radial velocity survey of 29 radio-selected mergers, and Golovich et al. (2019b, hereafter G19b) followed up with a panchromatic analysis including X-ray and radio data. Their subclustering analysis, based on $\approx 100-200$ spectroscopically confirmed member galaxies per system, revealed some of these systems to be multimodal, hence not amenable to modeling with halo pairs. Still, 15 systems were identified as bimodal, with the subclustering analysis providing best-fit central coordinates and velocities for each subcluster. This enables

Table 1
Cluster Parameters

Name	z	N^{a}	Subcluster 1		Subcluster 2	
			R.A. (J2000)	Decl.	R.A.	Decl.
ZwCl 0008.8+5215	0.10	103	00:12:02.5	52:34:00.9	00:11:32.5	52:30:35.3
A115	0.19	136	00:55:53.9	26:25:16.5	00:56:01.5	26:20:07.4
A523	0.10	114	04:59:13.2	08:49:45.0	04:59:05.2	08:43:37.5
A3411	0.16	215	08:41:51.7	-17:27:20.6	08:42:05.9	-17:34:01.8
RXC J1053.7+5452	0.07	75	10:53:35.5	54:52:07.5	10:54:08.5	54:49:48.0
A1240	0.19	86	11:23:36.9	43:09:08.6	11:23:37.0	43:03:13.7
PLCKESZ G287.0+32.9	0.38	111	11:50:49.7	-28:04:32.6	11:51:02.9	-28:12:27.4
A1612	0.18	52	12:47:34.6	-02:46:54.2	12:47:52.8	-02:49:37.6
RXC J1314.4-2515	0.25	133	13:14:34.5	-25:15:58.2	13:14:22.4	-25:16:24.5
ZwCl 1856.8+6616	0.30	45	18:56:35.8	66:21:14.8	18:56:31.7	66:25:04.5
A2443	0.11	145	22:26:01.1	17:23:48.1	22:26:09.7	17:20:47.7
CIZA J2242.8+5301	0.19	201	22:42:49.7	53:04:32.9	22:42:41.6	52:58:06.3

Note.

consistent TSP and $v_{\rm max}$ inferences for each of an ensemble of cluster mergers. Of these, ten systems at redshifts $z \leqslant 0.38$ have spectra that cover the H α line, an indicator of current star formation. These spectra also cover the nearby [N II] $\lambda 6583$ line, enabling us to separate those galaxies whose H α emission is related to an active galactic nucleus (AGN) rather than current star formation.

This paper revisits the spectroscopy of member galaxies in those clusters, extracting equivalent widths of the H α and [N II] λ 6583 lines to identify star-forming galaxies (SFGs) and AGN. We then examine whether the fraction or spatial distribution of SFG and/or AGN differs from that of other confirmed cluster members, and explore whether any such differences may be a function of the TSP or ν_{max} . The remainder of this paper is organized as follows: Section 2 describes our methods; Section 3, the results; and Section 4 provides discussion and interpretation.

2. Data and Methods

We focus on $H\alpha$ emission because it is a robust indicator of current star formation—see Kennicutt & Evans (2012) for a review—and because most of the clusters in the G19a spectroscopic survey were targeted over a wavelength range that includes $H\alpha$. Although the exact wavelength coverage varies from slit to slit in the G19a survey, nearly all slits that probe $H\alpha$ also probe [N II] λ 6583, allowing for discrimination between SFG and AGN as described below.

Cluster selection and geometry. We start with the 29 clusters in the G19a sample and select those for which G19a took spectra that went red enough to capture $H\alpha$ for cluster members. This excludes clusters beyond $z\approx 0.38$; PLCKESZ G287.0+32.9 at z=0.38 is the highest-redshift cluster examined in this work. Next, following the subclustering results of G19b, we selected those systems that were determined to be bimodal. This yields the 12 merging systems listed in Table 1.

We are interested in investigating $H\alpha$ emission as a function of the position along the merger axis, so we use the subcluster separation vector to define an x coordinate on the sky. The point midway between the subclusters is defined as x=0, and the subclusters themselves define $x=\pm 1$. We do not use the center of mass to define x=0 because mass measurements are

not available for each subcluster. With this definition the sign of x is arbitrary, and our later analysis will account for that by taking the absolute value of x.

Slit targeting. The G19a slit targeting procedure probed cluster members with a wide range of properties. Five of the twelve clusters considered here were in the Sloan Digital Sky Survey (SDSS) footprint at the time of G19a targeting. For these systems (A115, A1240, A1613, A2443, and RXC J1053.7+5452) G19a used SDSS photometric redshifts, creating a "Sample 1" catalog consisting of galaxies within $\pm 0.05(1+z_{cluster})$ of the cluster redshift, with a higher priority for brighter galaxies. The DSIMULATOR³ slit targeting software filled the mask with as many Sample 1 targets as possible while avoiding slit collisions, then filled in the remainder of the mask with Sample 2 targets. For the systems with photometric redshifts, Sample 2 consisted of other SDSS galaxies, with a higher priority for brighter galaxies.

Targeting for the other seven systems used a red-sequence method based on photometry available at the time, including the POSS-II Digitized Sky Survey (Djorgovski et al. 1992) for ZwCl 1856.8+6616; Isaac Newton Telescope/Wide Field Camera data from van Weeren et al. (2011) for A523, A3411, ZwCl 0008.8+5215, and two CIZA J2242.8+5301 masks; and Subaru/SuprimeCam photometry for A1314, PLCKESZ G287.0+32.9, and the remaining two CIZA J2242.8+5301 masks. For these systems, Sample 1 consisted of bright (r < 22.5) red-sequence galaxies and Sample 2 consisted of faint (22.5 < r < 23.5) red-sequence galaxies. However, there was still a need for filler slits and these were filled with blue cloud galaxies. Furthermore, where galaxies with known redshift were not targeted to avoid duplication, this tended to deplete red-sequence galaxies from the sample.

Furthermore, the long axis of the $16' \times 4'$ DEIMOS subtends 1.3–5.0 Mpc depending on cluster redshift, with a median of 2.9 Mpc. This corresponds to 2–6 times the subcluster separation, extending well beyond the central regions where red-sequence galaxies dominate. Hence even where red-sequence selection was used for prioritization, the final sample includes a wide range of galaxy colors. This is illustrated by Figure 1, which shows Panoramic Survey Telescope and Rapid Response System (Pan-STARRS; Chambers et al. 2016)

^a Number of galaxies within $3\sigma_v$ of the systemic velocity.

http://www.ucolick.org/~phillips/deimos_ref/masks.html

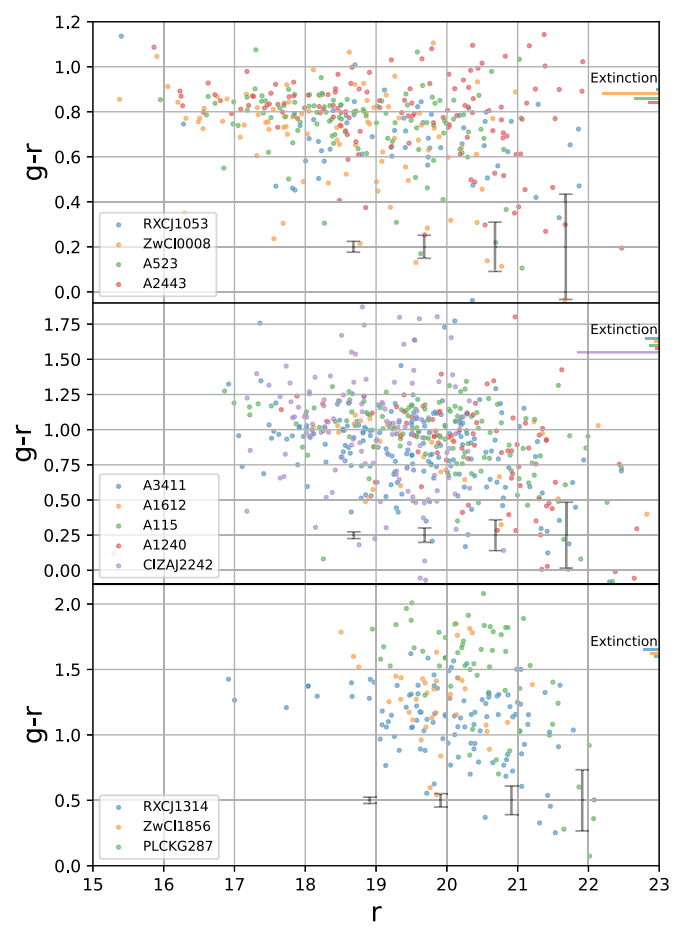


Figure 1. Pan-STARRS photometry of galaxies in the sample. The galaxies cover a wide range of luminosities and colors. Clusters are shown in order of increasing redshift, both within panels and across panels ($z \approx 0.10$, 0.19, and 0.30 from top to bottom). Colors have been dereddened; the extinction bars illustrate the widely varying extinction in the r band, which affects the depth to which obtaining a redshift is practical. Error bars show the typical color uncertainty at a given magnitude, taking into account the average extinction in a given panel; error bars smaller than the points have been omitted.

photometry for the sake of uniformity, specifically using g-r colors because those two filters straddle the 4000 Å break at these redshifts. Clusters are shown in order of increasing redshift, with clusters of similar redshift grouped in each panel ($z \approx 0.10$, 0.19, and 0.30 from top to bottom). The photometry has been dereddened using values from the extinction calculator provided by the NASA/IPAC Extragalactic Database⁴ (NED). The extinction in r is shown as a bar for each cluster, to help explain why some clusters seem to have shallower sampling than others; before dereddening, all clusters were similar in terms of the the faintest apparent magnitude at which a secure redshift was found.

In the low-redshift clusters, the galaxies sampled span a range of nearly seven magnitudes. At the other extreme PLCKESZ G287.0+32.9 is sampled over a more limited three-magnitude range due to its higher redshift (z=0.38), and CIZA J2242.8+5301 is sampled over a similarly limited range due to heavy extinction. The brightest galaxies sampled in each cluster have absolute r magnitudes of approximately -22.5. Sampling along the color axis spans a range of one magnitude or more in g-r. The red sequence clearly moves up in g-r with the

redshift, and even the dereddened CIZA J2242.8+5301 is consistent with this trend. However, the scatter in CIZA J2242.8+5301 is large after dereddening due to spatially varying extinction not modeled here. Setting that cluster aside, the range of colors sampled is still quite large. There is no clear correlation with the targeting scheme; for example, in the top panel, the two clusters with nominal red-sequence selection (A523 and ZwCl 0008.8+5215) clearly sample the blue cloud better than one of the two clusters with photometric redshift selection (RXC J1053.7+5452) and at least as well as the other (A2443). This illustrates how multiple factors (a large spatial footprint, the need to avoid slit collisions in dense regions, and so on) can diffuse the focus away from the red sequence even in those clusters with nominal red-sequence selection.

Data description. We provide a brief summary and refer readers to G19a for more details. Spectra were taken with the DEIMOS multiobject spectrograph (Faber et al. 2003) on the Keck II telescope at the W. M. Keck Observatory. The 1200 line mm⁻¹ grating was used with 1" slits, yielding a pixel scale of 0.33 Å pixel⁻¹, a resolution of ~1 Å or 50 km s⁻¹, and wavelength coverage spanning ≈2600 Å. For these lower-redshift clusters, the grating was tilted to ensure that Hα was captured, e.g., spanning 5400–8000 Å at a typical redshift of 0.2. Within a cluster, the wavelength coverage varied by ± 400 Å depending on the slit location. The DEEP2 versions of the spec2d and spec1d packages (Cooper et al. 2012; Newman et al. 2013) were used to remove instrumental artifacts, calibrate the wavelengths, and extract 1D spectra.

Equivalent width. The spectra were not photometrically calibrated and the slits capture only the central part of each galaxy, hence we do not attempt to extract $H\alpha$ luminosities. We rely on the equivalent width (EW), which compares the line to the surrounding continuum. This comparison has the additional virtue of being robust against dust in the emitting galaxy.

Using the galaxy redshifts determined by G19a, as well as the systemic redshifts and velocity dispersions σ_v from G19b, we selected cluster members as those within $3\sigma_{\nu}$ of the systemic velocity. We then created a nonparametric model of the continuum using an iterative smoothing procedure. Ideally, the smoothing is done after removing emission lines and other outliers such as bad pixels or residuals from subtracted sky lines. Our first pass removes the most intense 2.5% of pixels and the least intense 1.25% of pixels, then smooths using a boxcar kernel 400 pixels (132 Å) wide. These parameters were chosen for their robustness over a range of galaxy spectral types and signal-to-noise levels. The rms residuals from this first-pass model are then calculated, and outliers are defined as pixels whose first-pass residuals exceed 3 times this rms residual. The second pass smooths the original data with the same boxcar kernel, but now excluding outliers according to the above criterion.

The redshift of A3411 places the $H\alpha$ line in the 7600–7650 Å telluric absorption feature. The procedure described above was able to distinguish emitters and nonemitters, but often ascribed positive EW to the nonemitters, thus confusing $H\alpha$ absorption with telluric absorption. To avoid any bias in the EW measurements for this cluster we created an atmospheric transmission model using high signal-to-noise galaxies with no evident $H\alpha$ features. We then divided all A3411 spectra by this model before running the EW extraction procedure described above. With this correction in place, A3411 shows no more tendency to $H\alpha$ absorption than any

⁴ https://ned.ipac.caltech.edu/extinction_calculator

Table 2 $H\alpha$ Equivalent Width Estimates

R.A.	Decl.	EW (Å)	Uncertainty (Å)	
00:10:60.0	52:32:26.8	0.77	0.04	
00:11:05.6	52:32:60.0	2.21	0.17	
00:11:09.7	52:28:42.5	-26.19	0.43	
00:11:10.0	52:28:05.2	1.68	0.22	
00:11:10.6	52:31:00.1	0.88	0.11	
00:11:11.1	52:29:50.8	1.39	0.06	
00:11:12.2	52:31:40.6	-72.33	0.68	
00:11:13.0	52:30:52.1	-10.34	0.69	
00:11:13.1	52:29:58.8	1.76	0.29	
00:11:15.3	52:30:15.0	1.27	0.08	

(This table is available in its entirety in machine-readable form.)

other cluster. This correction had a negligible effect on the results described below, as emitters were already correctly identified.

We assess the uncertainty in the EW both empirically and with a noise model. The empirical method builds on the fact that the DEEP2 pipeline provides two different 1D extractions of the underlying 2D spectral trace. The "optimal" extraction follows the algorithm of Horne (1986) with modifications described in Newman et al. (2013), while the boxcar extraction uses a fixed width with a correction for the fraction of light falling outside that fixed width. Each 1D extraction has an accompanying per-pixel uncertainty estimate. Both extractions rely on the same 2D spectrum so they are not statistically independent; rather the extraction comparison is designed to highlight systematic differences. For example, the two extractions differ visibly near the end of the observed wavelength range, which becomes important for clusters where H α lies near the end of that range. Different realizations of the continuum could interact with our iterative continuum modeling procedure in complicated ways, so we measure the EW from each extraction and compare. For 68% (95%) of the galaxies, the two EW estimates were within 0.19 (3.5) Å. Looking more closely at galaxies where the two EW estimates disagreed by more than 2 Å (60 of the 746 galaxies, or 8%) we found the vast majority of these to be strong emitters for which this was a small fractional error. We conclude that uncertainties related to extraction do not impair our ability to classify galaxies as emitters or nonemitters (we consider the few ambiguous cases in more detail below). We adopt the mean of the two EW estimates as our final EW estimate.

Our noise model uses the propagation of uncertainties from the per-pixel uncertainties, assuming the analytically tractable case of modeling the continuum as linear. In this limit, we find that the dominant error for most slits arises from uncertainty in the pixels representing ${\rm H}\alpha,$ rather than in the continuum estimation. For 85% of slits, the uncertainty calculated this way is larger than the difference between the two extractions, which is consistent with (i) the dominant uncertainty arising from pixel statistics rather than systematics and (ii) the two extractions not being statistically independent. Hence we adopt the (usually more conservative) uncertainties provided by the noise model. The galaxy coordinates, EW, and uncertainties $\sigma_{\rm EW}$ are listed in Table 2.

Emitter/nonemitter classification. Figure 2 shows a histogram of $H\alpha$ EW measurements across all clusters and member

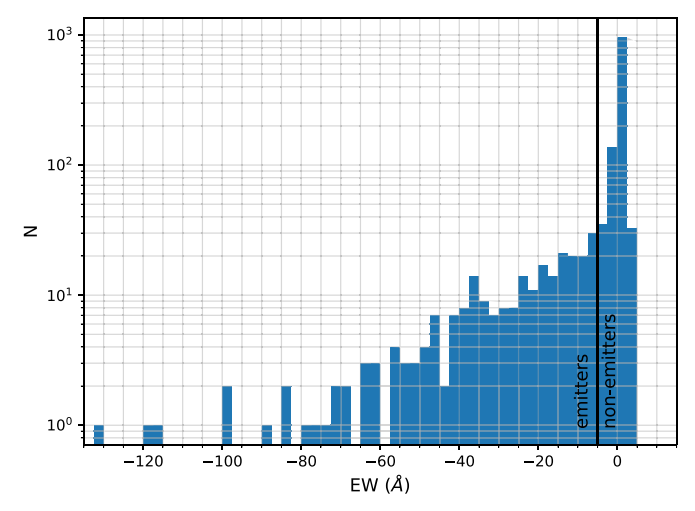


Figure 2. Histogram of $H\alpha$ EW measurements across all clusters and member galaxies.

galaxies. The distribution has a nearly symmetric peak around zero with a long tail toward negative (emitting) values. The distinction between the peak (whose width is determined by noise) and the tail of emitters begins at an EW of -5 Å. Therefore, we define three categories:

- 1. emitters: EW + 5 Å < $-\sigma_{\rm EW}$
- 2. nonemitters: EW + 5 Å > $\sigma_{\rm EW}$
- 3. ambiguous: $|EW 5 \text{ Å}| < \sigma_{EW}$

where $\sigma_{\rm EW}$ is the EW uncertainty of a given galaxy. Of 1390 member galaxies, this yielded 1173 galaxies classified as nonemitters, 240 as emitters, and 13 as ambiguous.

SFG/AGN classification. H α emission may be due to star formation or to AGN activity. Line ratios are useful in distinguishing the two (Baldwin et al. 1981; Carter et al. 2001). Based on Figure 10 of Carter et al. (2001) we adopt the categories:

- 1. $\log_{10}[N \text{ II}]6583/H\alpha < -0.3$: star-forming galaxy
- 2. $-0.3 < \log_{10}[N \text{ II}]6583/H\alpha < -0.25$: ambiguous
- 3. $\log_{10}[N \text{ II}] \frac{6583}{H\alpha} > -0.25$: AGN

Of 1390 cluster members with spectra supporting H α and [N II] measurements, we find 240 H α emitters, of which 197 are classified as SFG and 37 as AGN, with six ambiguous.

Dynamical modeling. We use the method of Wittman (2019) to infer TSP, the maximum relative velocity reached around the time of pericenter v_{max} , and the viewing angle θ (defined as 90° for a subcluster separation vector in the plane of the sky) for each system. In this method, halo pairs at the appropriate redshift are identified in the Big Multidark Planck (BigMDPL) Simulation (Klypin et al. 2016). These pairs are then tracked back in time to ensure that they have had one pericenter passage by the observed redshift because each observed system has radio relics and X-ray morphology that require at least one pericenter passage but are unlikely to persist after two such passages. Each halo pair meeting this requirement is referred to as an analog. Each analog is then "observed" from 2627 lines of sight distributed over a sphere, each line of sight defined by a colatitude θ and an azimuth ϕ , defined with respect to the subcluster separation vector. The inclusion of ϕ is an important detail relative to more analytical methods which assume a velocity vector parallel to the separation vector, or in other words a perfectly head-on collision.

Table 3
Inferred Merger Dynamical Parameters

Name	,	ΓSP	1	$v_{ m max}$	View Angle (deg, 68% CI)
	(Myr)	68% CI	$(km s^{-1})$	68% CI	
A115	346	215–451	1978	1772–2172	68-90
A523	510	331-632	2377	1995–2618	58-86
A1240	451	195-577	2254	1979–2466	64–88
A1612	638	447-782	2544	2372-2908	70-90
A2443	277	156-381	1977	1521-2194	72–90
A3411	755	476-971	2544	2194-2808	72-90
CIZA J2242.8+5301	608	378-937	2629	2403-2808	68-90
PLCKESZ G287.0+32.9	519	341-812	2586	2263-3091	68-88
RXC J1053.7+5452	270	125-351	1954	1521-2203	66–88
RXC J1314.4-2515	206	100-328	2350	2018–2653	26-62
ZwCl 0008.8+5215	802	516-897	2360	2020-2461	72-90
ZwCl 1856.8+6616	446	50-627	2416	2036-2749	66–90

The observables are simple: the projected separation between subclusters; the relative line-of-sight velocity between subclusters (as measured by member galaxy redshifts); and subcluster masses where available. The likelihood of each (analog, θ , ϕ) tuple is computed. The likelihood for θ is then computed by marginalizing over analogs and over ϕ . (Other methods assuming a relative velocity parallel to the separation vector must—wrongly—place the separation vector away from the plane of the sky if the observed component of the relative velocity vector is nonzero; by marginalizing over ϕ this method correctly handles that common situation.) The likelihood for TSP (ν_{max}) is computed by assigning a TSP (ν_{max}) to each analog and marginalizing over θ and ϕ .

For the observed values and uncertainties, we used the values from G19b. This sample has substantial overlap with that of Wittman (2019), but that work included only the G19b "gold sample" which focused on systems with double radio relics. Table 3 presents the inferred parameter values and confidence intervals (CI).

3. Results

Fraction of SFG and AGN. Figure 3 plots the fraction of members classified as SFG versus TSP, with each TSP shown as a probability density function. Although the TSP distributions overlap, there is enough distinction between young and old mergers to support visualization of a trend should it exist, but no trend is evident. The spectroscopic targeting was focused on confirming likely cluster members based in part on color, so the overall fraction of galaxies found to be emitters is likely to be biased low; we defer discussion of this issue to Section 4.

Figure 4 plots the fraction of members classified as AGN versus TSP. Again, no trend is evident. The reader may note that A1240 is high in both the SFG fraction and the AGN fraction. This raises the question of whether clusters with high SFG fractions tend to also have high AGN fractions. We find that this is not the case (p = 0.84 for the null hypothesis of no correlation).

The pericenter speed estimates of various clusters overlap even more than the TSP estimates, but for completeness, we plot the SFG and AGN fractions versus pericenter speed v_{max} in Figures 5 and 6. There is no evident trend.

Spatial distribution of SFG and AGN. Spectroscopic targeting biases (such as slit collisions preventing full sampling

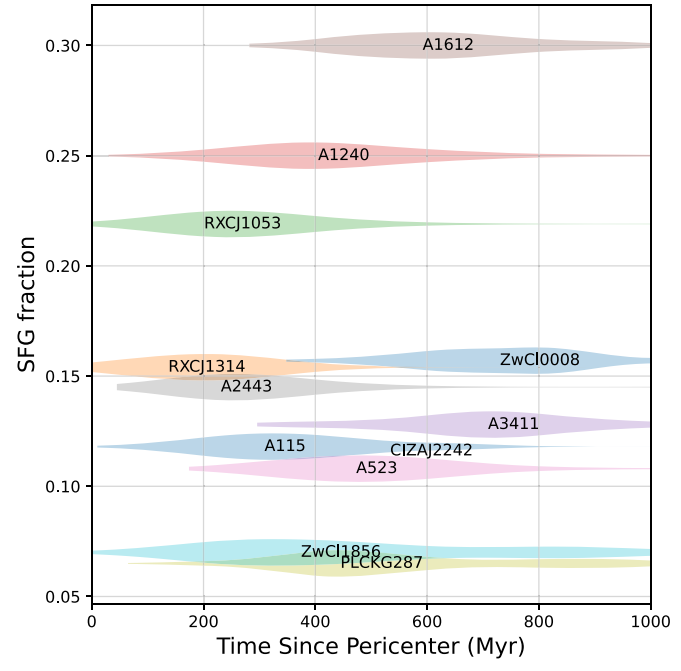


Figure 3. SFG fraction vs. time since pericenter. No trend is evident.

of the densest cluster regions) are likely to affect emitters and nonemitters equally. Therefore we compare the spatial distribution of SFG and AGN in a given system with the spatial distribution of nonemitters in the same system. Figure 7 shows the cumulative distribution function (CDF) of the absolute value of x, in other words, the distance of each galaxy from the center of the merging system, projected along the subcluster separation vector. Hence, the shaded area represents the region between the subclusters' centers.

In most systems, the distributions of emitters and none-mitters are qualitatively similar. However, there are some notable variations. For A523, A2443, RXC J1053.7+5452, and RXC J1314.4–2515 the SFG CDF is consistently lower than the nonemitter CDF, meaning that SFG tend to reside at larger projected distances from the system center. In three of these four systems, the paucity of AGN prevents us from assessing whether AGN are distributed more like the nonemitters or the SFG. However, RXC J1314.4–2515 has sufficient AGN to see that they are distributed similarly to the SFG rather than the nonemitters.

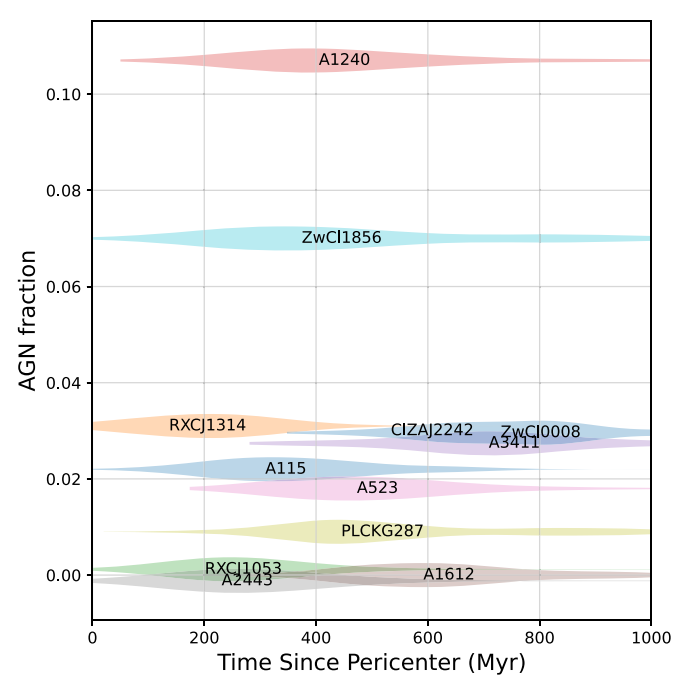


Figure 4. AGN fraction vs. time since pericenter. No trend is evident.

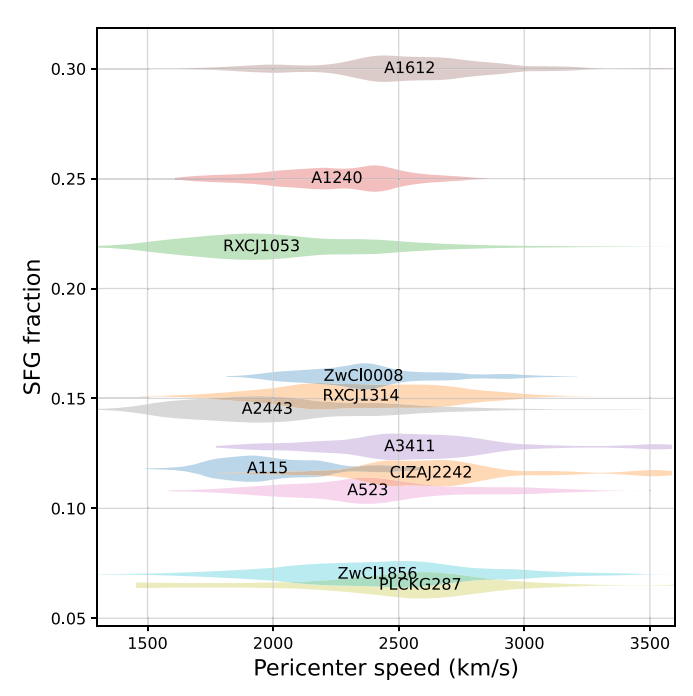


Figure 5. The SFG fraction shows no trend with pericenter speed. Small vertical shifts (0.003 or less) have been applied to some clusters for clarity.

It is difficult to find a counterexample: a system in which the SFG and/or AGN are more centrally concentrated than the general population. ZwCl 0008.8+5215 shows hints of both SFG and AGN being more centrally concentrated, but this is not significant according to the test described below. In A1240 the AGN distribution appears more centrally concentrated, but this has marginal significance as described below.

To test the significance of any discrepancy between distributions we employ the Anderson-Darling test which is a more sensitive version of the classic Kolmogorov-Smirnov test for consistency between two distributions (Feigelson & Babu 2012). We use the scipy.stats.anderson_ksamp

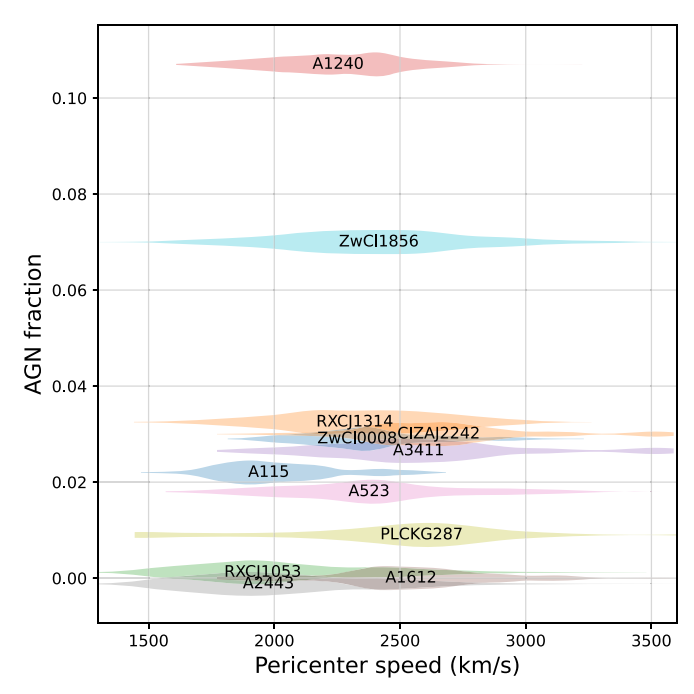


Figure 6. The AGN fraction shows no trend with pericenter speed. Small vertical shifts (0.002 or less) have been applied to some clusters for clarity.

routine, which returns a truncated range of p-values between 0.001 (highly significant) and 0.25 (no significance). These values are displayed in each panel of Figure 7. The four systems with far-flung SFG listed above indeed have SFG distributions inconsistent (p < 0.01) with their nonemitter distributions. Testing for consistency between AGN and nonemitter distributions, we find one system, A1240, with a mild (p = 0.053) tendency for centrally concentrated AGN, and one, RXC J1314.4–2515, with a stronger (p = 0.019) tendency for far-flung AGN. In the latter system, the AGN distribution is consistent with the far-flung SFG distribution; the other three systems with far-flung SFG had too few AGN to support a meaningful test.

Relating SFG distribution to dynamical parameters. The two clusters with the lowest TSP (RXC J1053.7+5452 and RXC J1314.4–2515) have significantly far-flung SFG while the cluster with the highest TSP (ZwCl 0008.8+5215) has SFG more centrally concentrated than nonemitters (albeit not significantly so). Hence, a natural hypothesis is that the SFG distribution is affected by TSP.

Figure 8 plots the SFG *p*-value versus TSP. The vertical axis is defined such that systems with highly inconsistent SFG and nonemitter distributions appear toward the bottom of this plot. Of the four systems with standout SFG distributions, three of them are also the three youngest systems. RXC J1314 in particular is both the youngest system and the system with the most significant discrepancy between emitter and nonemitter distribution, at the *p*-value floor of 0.001. These examples suggest that the SFG distribution may change with TSP, but the case is far from clear: the fourth standout SFG distribution, A523, is middle aged. We also tested the SFG distribution as a function of the radius from the center of the system (projected on the sky) rather than along the merger axis. The results show slightly weaker evidence for a trend with projected radius.

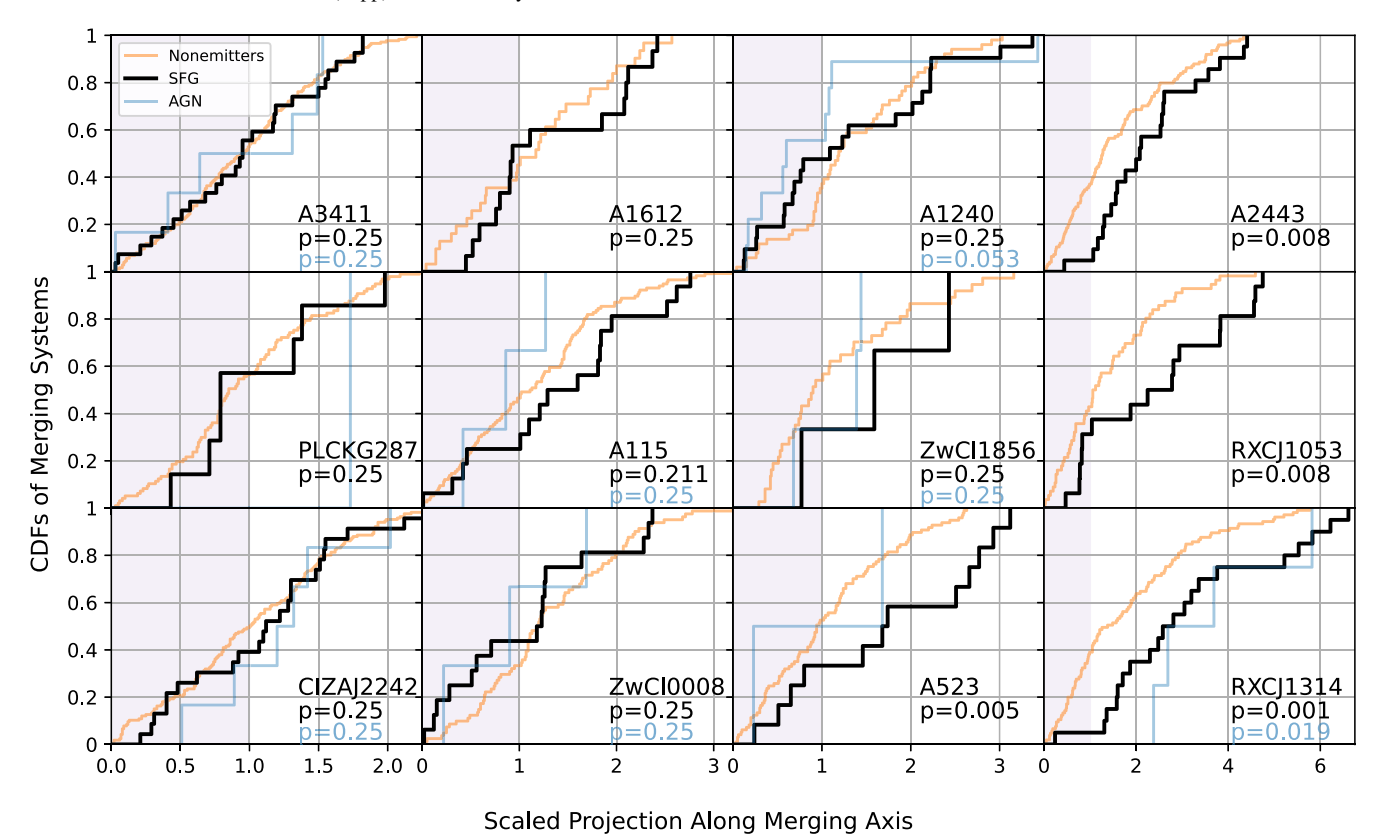


Figure 7. SFG and AGN vs. nonemitter spatial distribution for each of the merging systems. The distance along the merging axis is defined as zero at the center of the system and one at each of the subclusters, hence the shaded area represents the region between the subclusters. *P*-values are given for Anderson–Darling tests of SFG (black) and AGN (blue) consistency with the nonemitter distribution. For systems with two or fewer AGN, no AGN *p*-value is computed.

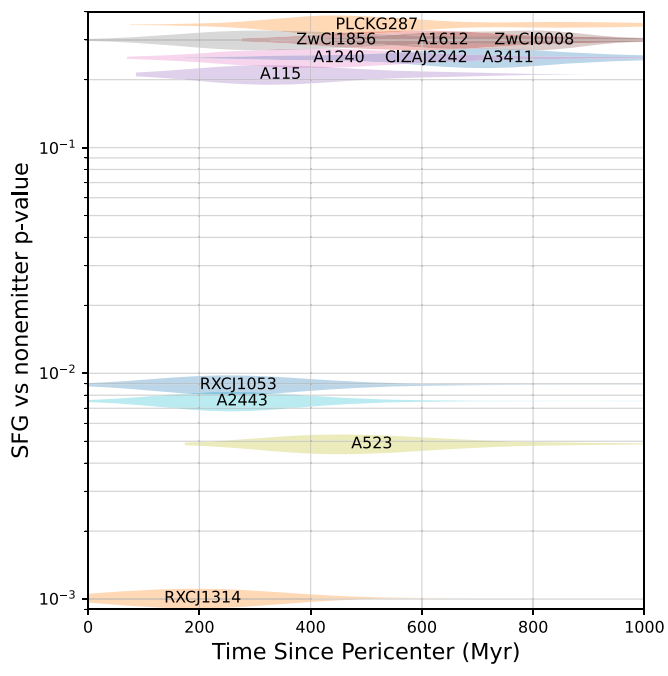


Figure 8. *P*-value (measuring agreement between the spatial distributions of SFG and of nonemitters) vs. TSP for each system. Lower p-values indicate that the SFG distribution along the merger axis differs from that of nonemitters. P-values are truncated to the interval [0.001, 0.25]; the seven systems with entirely consistent distributions (p = 0.25) are shown with slight vertical displacements for clarity.

Figure 9 plots the SFG *p*-value versus the other dynamical parameter, pericenter speed. The four systems with standout SFG distributions are evenly split between low and moderate pericenter speeds.

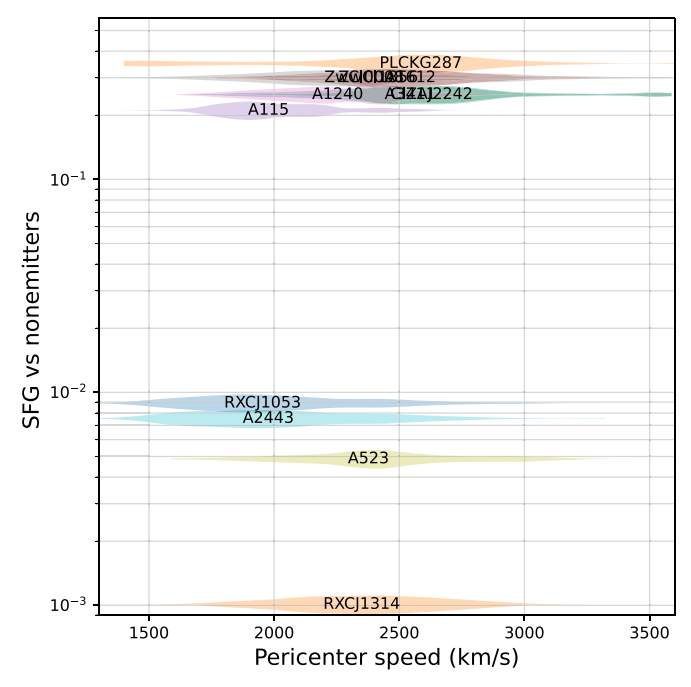


Figure 9. SFG spatial distribution vs. pericenter speed. See Figure 8 for details.

Relating AGN distribution to dynamical parameters. Figure 10 probes the relationship between TSP and the spatial distribution of AGN. The cluster with the lowest TSP (RXC J1314.4–2515) also has the most discrepant AGN distribution. However, other clusters with low TSP (A2443 and RXC J1053.7+5452), which like RXC J1314.4–2515 had far-flung

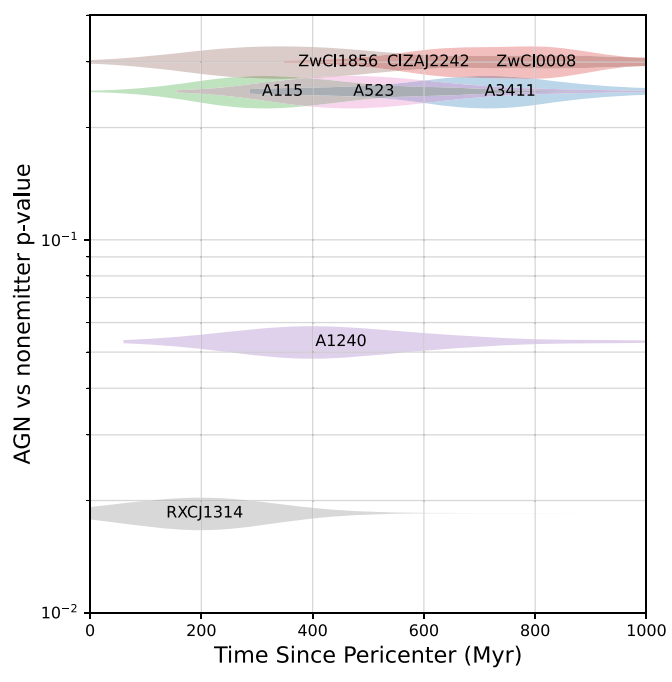


Figure 10. *P*-value (measuring agreement between the spatial distributions of AGN and of nonemitters) vs. TSP for each system. Lower *p*-values indicate that the AGN distribution along the merger axis differs from that of nonemitters. *P*-values are truncated to the interval [0.001, 0.25]; the six systems with entirely consistent distributions (p = 0.25) are shown with slight vertical displacements for clarity. Note that four systems have too few AGN to quantify their distribution along the merger axis.

SFG distributions, have too few AGN to probe their AGN spatial distribution. Hence, any suggested relation between AGN spatial distribution and TSP rests largely on the single example of RXC J1314.4–2515.

Figure 11 probes the relationship between AGN spatial distribution and the other dynamical parameter, pericenter speed. Here, there is not even a hint of a trend, as the two clusters with measurably far-flung AGN distributions have unremarkable pericenter speeds.

4. Discussion

Timescales. H α emission is an indicator of very recent (past ~20 Myr; Kennicutt 1998; Kennicutt & Evans 2012) star formation. This is a much shorter timescale than the TSP in this sample, which ranges from 200 to 800 Myr. Hence, these data are not intended to probe any star formation that may have been triggered and quenched earlier in the merger process. Such questions are better probed by using other spectral indicators (Mansheim et al. 2017a, 2017b), combining morphology and photometry with spectroscopy (Ma et al. 2010), or possibly stellar population synthesis modeling of member galaxies. The narrow time window for $H\alpha$ emission is well suited to a complementary question: where are the merger effects, if any, being felt now? A cluster merger is not a single event but a long process that may affect different regions at different times. In particular, pericenter passage initiates the launch of a shock that, even at $\sim \! 3000 \, \mathrm{km \, s^{-1}}$, still takes 300 Myr or more to travel 1 Mpc into the cluster outskirts. The 16' DEIMOS field, corresponding to a 3.1 Mpc diameter at the median redshift of our sample, is well suited to probing both shocked and unshocked regions.

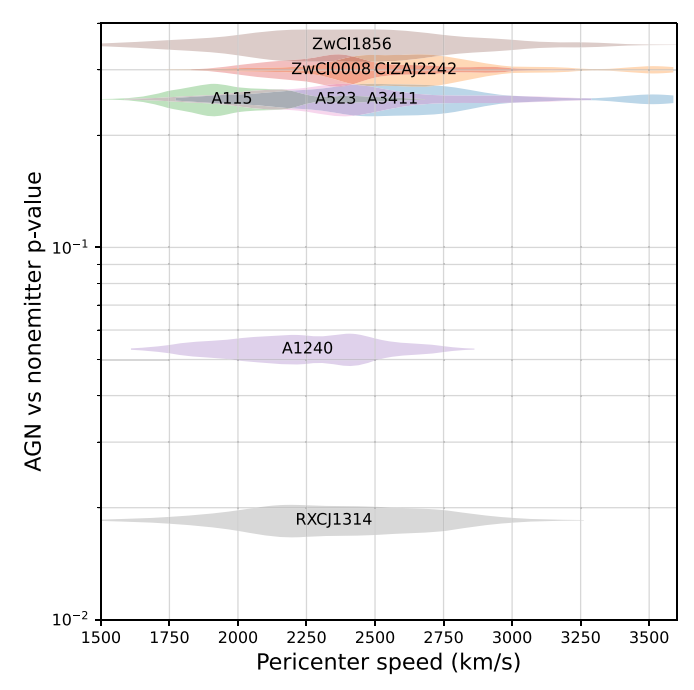


Figure 11. AGN spatial distribution vs. pericenter speed. See Figure 10 for details

Another relevant timescale is the galaxy dispersion timescale. Consider each subcluster as an isolated unit with member galaxies having random speeds of order $1000~\rm km~s^{-1}$ along any given direction x on the sky. As a concrete example, if star formation were triggered only at the time and location of the pericenter, when viewed 500 Myr later the affected galaxies would be dispersed over a 1 Mpc diameter window along the merger axis. This makes it difficult to reconstruct events that happened around the time of the pericenter, even if detailed and reliable star formation histories were extracted from all member galaxies. The limited time window relating $H\alpha$ emission to star formation is actually an advantage in this regard: $H\alpha$ is emitted promptly at the time and location of star formation.

Potential systematic and physical effects. The fraction of slits with SFG varies widely, from 0.065 (PLCKESZ G287.0+32.9) to 0.30 (A1612), but there is no correlation between SFG fraction and TSP or v_{max} . Similar statements apply to the fraction of slits with AGN, and to the fraction of slits with $H\alpha$ emitters of any type. This raises the question of what controls the emitter fraction. Slit targeting may play a role. For seven systems, masks were designed based on two-band photometry with priority placed on red-sequence galaxies, while the other five systems were based on SDSS photometry and photometric redshifts, which increased the likelihood of targeting member galaxies outside the red sequence. Figure 12 plots the emitter fraction using different symbol types for the two types of slit targeting. Indeed, the three highest emitter fractions are in systems with photometric redshift targeting. Even in redsequence masks, however, one-third to perhaps one-half of the slits were filler slits of bluer galaxies with magnitudes appropriate to cluster members. This explains the substantial overlap in emitter fraction between the two sets of targets in Figure 12.

Nevertheless, one can ask whether there are trends within each subset. Figure 12 shows no obvious redshift trend within either subset. This is perhaps surprising: given the fixed DEIMOS field of view (approximately $16^{\prime} \times 5^{\prime}$, with the long

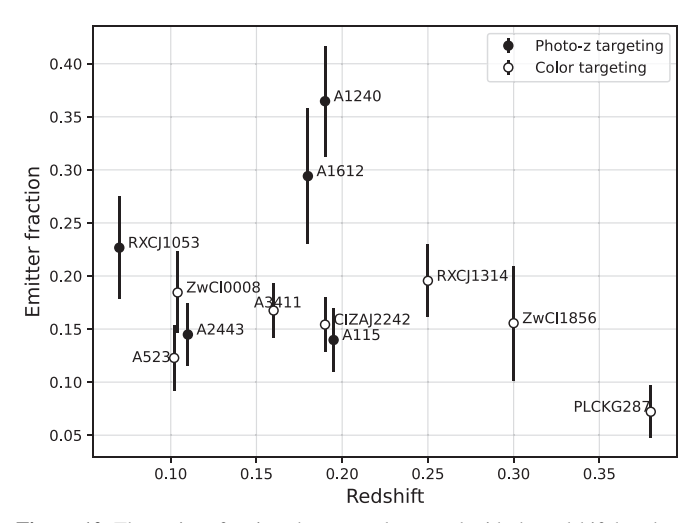


Figure 12. The emitter fraction shows no clear trend with the redshift but does appear to be lower with color selection, as expected if most slits are assigned to red-sequence galaxies. Uncertainties assume a binomial process operating independently in each cluster.

dimension placed along the subcluster separation vector), higher-redshift systems are probed to larger physical radii where more emitters may be expected.

Next, we consider the spatial distribution of SFG and AGN compared to nonemitters in the same system, focusing on SFG due to the paucity of AGN. Figure 7 shows clear variations from system to system. Figure 8 suggests a potential association with TSP, but the evidence is weak. Note that slit targeting effects seem to play no role here: the four systems with discrepant emitter distributions are evenly split between color and photometric redshift targeting methods. We also checked for an association with the redshift and found none. It is possible that other merger parameters, such as pericenter speed, have an effect, but the uncertainties on the pericenter speed are currently too large to differentiate clearly between slow and fast mergers.

What other effects could play a role in the SFG distribution? Figure 7 does show that the systems with far-flung SFG distributions tend to be those in which the spectroscopic footprint, in units of the projected subcluster separation, is larger. The physical field size effect discussed above is not at play here, again because that would cause a clear redshift trend that is not seen here. In fact, the highest-redshift cluster, PLCKESZ G287.0+32.9, is an illustrative counterexample: it is probed out to a large physical radius, but a fairly small radius in units of subcluster separations, and it shows no SFG/nonemitter discrepancy.

Perhaps the subcluster separation sets a spatial scale that affects the SFG distribution. One possible mechanism is the shock generated at the pericenter passage. The shock outruns the subclusters but not by a large factor, at least in the first $\sim\!200\,\mathrm{Myr}$ (Springel & Farrar 2007), so the subcluster separation may be providing a rough scale for the shock separation. However, this does not explain why, in three of the four systems with standout SFG distributions, the SFG and nonemitter distributions start diverging *within* one subcluster separation.

Early versus late-type galaxies. Merger effects on galaxies likely depend on galaxy type. While a full exploration is beyond the scope of this paper, we address one potential systematic effect here: does the selection of many red-sequence

galaxies (thought to be relatively immune to star formation triggers) lead predictably to a null result? We note that most mergers examined here have no dearth of SFG projected near the subcluster cores (x=1 in our coordinate system), where red-sequence galaxies tend to congregate. The fact that SFG⁵ are typically found in these regions suggests that the G19a slit selection did not result in low sensitivity to star formation activity. The question is rather: what is different about the four systems with star formation activity located further out? As noted above, slit targeting differences are not an explanatory variable. Figure 1 suggests that variations in color sampling and depth are also not explanatory.

Relation to shock. We checked the four systems with farflung star formation activity against the G19b diagrams of these systems, illustrating radio relic positions (assumed to be tracing a shock) relative to the subclusters, and we found no commonality. Three of the systems have single relics and one (RXC J1314.4–2515) has double relics, a ratio consistent with the G19b sample as a whole. Two of the systems (A523 and A2443) have shocks projected more or less at the subcluster position (x = 1 in our coordinate system), while the other two have relics projected much further out ($x \approx 4$ for RXC J1053.7 +5452 and RXC J1314.4–2515, with the latter cluster also having a second relic projected at $x \approx 2.5$). RXC J1314.4–2515 is noted as having substantial line-of-sight velocity difference between the subclusters; the others are not, a ratio consistent with the G19b sample as a whole.

Relation to other results. Sobral et al. (2015) proposed a link between the shock and H α emitters in CIZA J2242.8+5301. They used narrow-band imaging to select candidate emitters and confirmed 83 H α emitters spectroscopically, most with the AutoFib2+WYFFOS (AF2) instrument on the William Herschel Telescope. The DEIMOS spectra used here serendipitously provided confirmation for 26 of their emitter candidates. The AF2 instrument covers a much larger field, with an unvignetted field of 20' radius, and the fibers were targeted specifically at narrow-band emitter candidates. Hence, the Sobral et al. (2015) data set provides a complementary view of CIZA J2242.8+5301 despite some overlap in spectroscopic data. They propose that H α emitters "are found preferably near the shock fronts" but this is not evident in our (more limited) view of the same cluster. If emitters had a preferred location (relative to nonemitters) their CDFs in Figure 7 would look more like sigmoid functions, rising sharply at the preferred location. The most plausible example of such a rise in Figure 7 is for ZwCl 0008.8+5215, indeed just outside the subcluster separation. However, this rise represents only five SFG.

One caveat in our analysis is that we have not adopted a center-of-mass (CM) coordinate system because the subcluster masses are not all known. It is possible that a CM analysis would allow for some pattern to emerge. However, we note that CIZA J2242.8+5301 has subclusters of roughly equal mass (Jee et al. 2015) so a CM analysis would not substantially change our result for that cluster.

Based on narrow-band imaging, Stroe et al. (2015) found that CIZA J2242.8+5301 "has an H α emitter density >20 times that of blank fields" and Stroe et al. (2017) found that merging clusters have double the H α emitters of relaxed clusters. This is compatible with our results, as we do not

⁵ The morphological types of these emitters may be a topic for future work; we simply note here that projection effects and slit targeting effects allow for the possibility that these emitters are not necessarily early-type galaxies.

compare to nonmerging clusters or the field, merely to nonemitters in the same merging cluster. Stroe et al. (2017) also found that ϕ^* , the characteristic density of the $H\alpha$ luminosity function, drops from the cluster core to the outskirts. This is also compatible with our results because the nonemitter density also drops from the cluster core to the outskirts. In most of our systems, these two densities drop at a similar rate, but in some systems (A523, A2443, RXC J1053.7+5452, and RXC J1314.4–2515) the density of nonemitters actually drops faster than that of $H\alpha$ emitters, resulting in more far-flung emitters than the general population targeted for slits. After classifying emitters as SFG or AGN, we find that this statement remains true for SFG in all four of those systems, and for AGN in the one system (RXC J1314.4–2515) with sufficient AGN to make a statement.

In conclusion, these data are suggestive that in systems viewed soon (\approx 200 Myr) after pericenter, H α emitting galaxies are less centrally concentrated than nonemitting member galaxies in our spectroscopic sample. However, this is based on three merging systems, and a fourth system with a larger TSP also exhibits this behavior. Probing this potential link further will require more precise TSP estimates and more mergers with TSP in the range of 0–400 Myr. The H α emitters we find are overwhelmingly SFGs, such that AGN distributions are often unconstrained by these data. Nevertheless, it is worth noting that in the one low-TSP system where the AGN distribution can be constrained, it agrees with the SFG distribution rather than the nonemitter distribution.

Acknowledgments

We thank the anonymous referee for several insightful suggestions. We thank Rodrigo Alves Stancioli for numerous suggestions and corrections. This work was supported in part by NSF grant 2308383. The data presented herein were obtained at the W.M. Keck Observatory, which is operated as a scientific partnership among the California Institute of Technology, the University of California, and the National Aeronautics and Space Administration. The Observatory was made possible by the generous financial support of the W.M. Keck Foundation. Funding for the DEEP2/DEIMOS pipelines has been provided by NSF grant AST-0071048. The DEIMOS spectrograph was funded by grants from CARA (Keck Observatory) and UCO/Lick Observatory, an NSF Facilities and Infrastructure grant (ARI92-14621), the Center for Particle Astrophysics, and by gifts from Sun Microsystems and the Quantum Corporation. Part of this work was performed under the auspices of the U.S. Department of Energy by Lawrence Livermore National Laboratory under Contract DE-AC5207NA27344. This research has made use of NASA's Astrophysics Data System. This research has made use of the NASA/IPAC Extragalactic Database (NED), which is funded by the National Aeronautics and Space Administration and operated by the California Institute of Technology.

Facility: Keck:II.

ORCID iDs

References

```
Baldwin, J. A., Phillips, M. M., & Terlevich, R. 1981, PASP, 93, 5
Carter, B. J., Fabricant, D. G., Geller, M. J., Kurtz, M. J., & McLean, B. 2001,
   ApJ, 559, 606
Chambers, K. C., Magnier, E. A., Metcalfe, N., et al. 2016, arXiv:1612.05560
Chung, S. M., Gonzalez, A. H., Clowe, D., Markevitch, M., & Zaritsky, D.
  2010, ApJ, 725, 1536
Cooper, M. C., Newman, J. A., Davis, M., Finkbeiner, D. P., & Gerke, B. F.,
   2012 spec2d: DEEP2 DEIMOS Spectral Pipeline, Astrophysics Source
  Code Library, ascl:1203.003
Dawson, W. A. 2013, ApJ, 772, 131
Djorgovski, S., Lasker, B. M., Weir, W. N., et al. 1992, AAS Meeting
  Abstracts, 180, 13.07
Faber, S. M., Phillips, A. C., Kibrick, R. I., et al. 2003, Proc. SPIE, 4841, 1657
Feigelson, E. D., & Babu, G. J. 2012, Modern Statistical Methods for
   Astronomy (Cambridge: Cambridge Univ. Press)
Golovich, N., Dawson, W. A., Wittman, D. M., et al. 2019a, ApJS, 240, 39
Golovich, N., Dawson, W. A., Wittman, D. M., et al. 2019b, ApJ, 882, 69
Horne, K. 1986, PASP, 98, 609
Jee, M. J., Stroe, A., Dawson, W., et al. 2015, ApJ, 802, 46
Kahn, F. D., & Woltjer, L. 1959, ApJ, 130, 705
Kennicutt, R. C., & Evans, N. J. 2012, ARA&A, 50, 531
Kennicutt, R. C., Jr. 1998, ApJ, 498, 541
Klypin, A., Yepes, G., Gottlöber, S., Prada, F., & Heß, S. 2016, MNRAS,
  457, 4340
Ma, C. J., Ebeling, H., Marshall, P., & Schrabback, T. 2010, MNRAS,
  406, 121
Mansheim, A. S., Lemaux, B. C., Dawson, W. A., et al. 2017a, ApJ, 834, 205
Mansheim, A. S., Lemaux, B. C., Tomczak, A. R., et al. 2017b, MNRAS,
   469, L20
Miller, N. A., & Owen, F. N. 2003, AJ, 125, 2427
Molnar, S. 2016, FrASS, 2, 7
Navarro, J. F., Frenk, C. S., & White, S. D. M. 1997, ApJ, 490, 493
Newman, J. A., Cooper, M. C., Davis, M., et al. 2013, ApJS, 208, 5
Sobral, D., Stroe, A., Dawson, W. A., et al. 2015, MNRAS, 450, 630
Springel, V., & Farrar, G. R. 2007, MNRAS, 380, 911
Stroe, A., Sobral, D., Dawson, W., et al. 2015, MNRAS, 450, 646
Stroe, A., Sobral, D., Paulino-Afonso, A., et al. 2017, MNRAS, 465, 2916
van Weeren, R. J., Röttgering, H. J. A., & Brüggen, M. 2011, A&A, 527, A114
Wittman, D. 2019, ApJ, 881, 121
Wittman, D., Cornell, B. H., & Nguyen, J. 2018, ApJ, 862, 160
```